Supplementary Information

The role of Tyr34 in proton-coupled electron transfer and product inhibition of manganese superoxide dismutase

Jahaun Azadmanesh[1], Katelyn Slobodnik[1], Lucas R. Struble[1], Jeffrey J. Lovelace, Erika A. Cone[1], Medhanjali Dasgupta[1], William E. Lutz[1], Siddhartha Kumar[1], Amarnath Natarajan[1], Leighton Coates[2], Kevin L. Weiss[3], Dean A. A. Myles[3], Thomas Kroll[4], and Gloria E. O. Borgstahl[1]*

[1]Eppley Institute for Research in Cancer and Allied Diseases, 986805 Nebraska Medical Center, Omaha, NE 68198-6805, USA

[2]Second Target Station, Oak Ridge National Laboratory, 1 Bethel Valley Road, Oak Ridge, TN 37831, USA

[3]Neutron Scattering Division, Oak Ridge National Laboratory, 1 Bethel Valley Road, Oak Ridge, TN 37831, USA

[4]Stanford Synchrotron Radiation Lightsource, SLAC National Accelerator Laboratory, Menlo Park, CA 94025, USA

*gborgstahl@unmc.edu

Supplementary Information Table of Contents

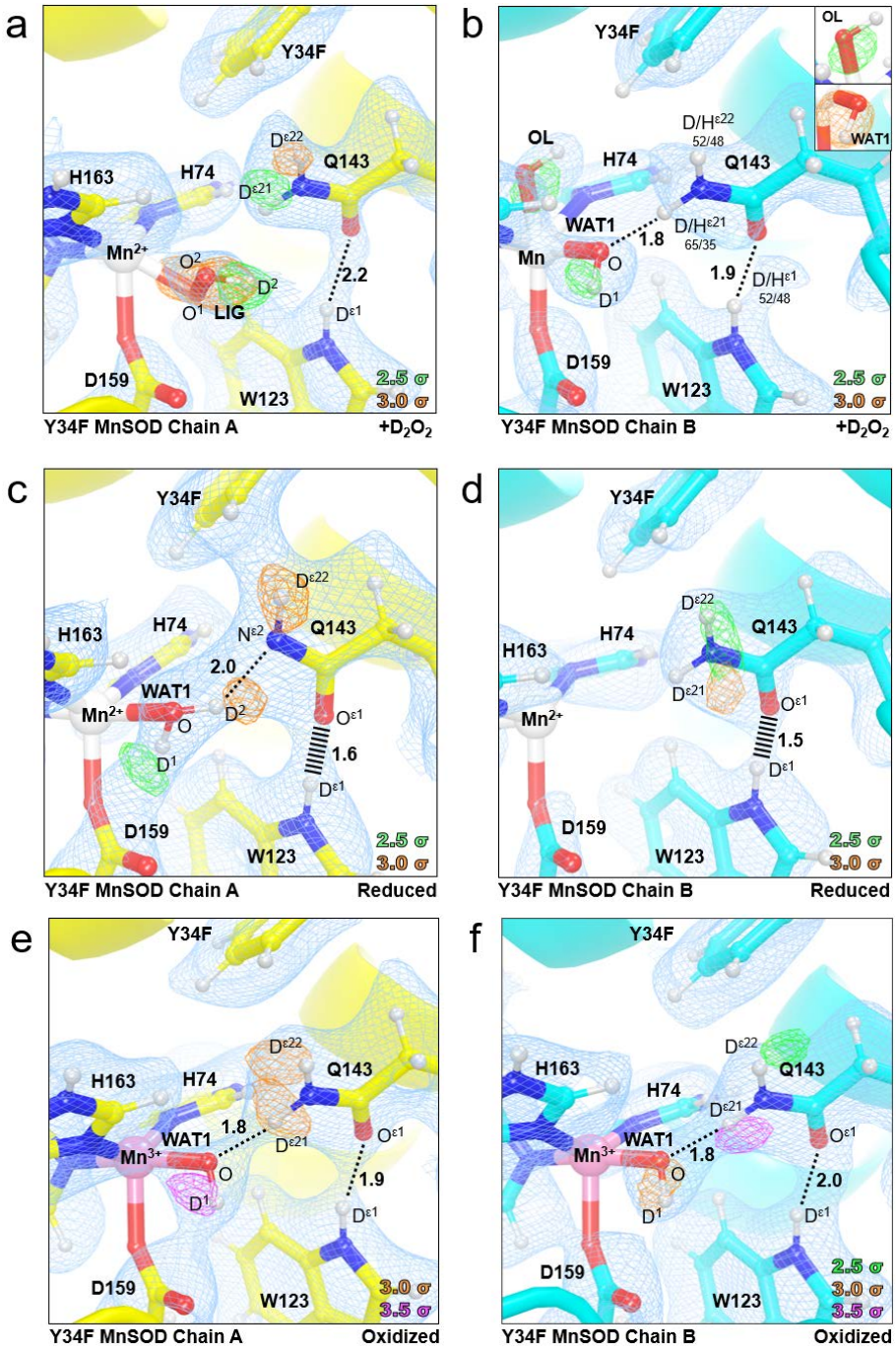

Supplementary Figure 1: Neutron structure and protonation states at the active sites of D2O2-soaked, reduced, and oxidized Tyr34Phe MnSOD. a-b Neutron structure of D_2O_2-soaked Tyr34Phe MnSOD. For the exchangeable protons of Gln143 and Trp123 of chain B, positive omit difference density was not present above 2.0σ due to density cancellation with hydrogen's negative neutron scattering length density. As an alternative, the proton positions were refined for H/D occupancy. Furthermore, an omit density for a hydroxide ion was observed to be bound to the Mn ion, opposite Asp159 (part b, inset top). WAT1 was interpreted to be a hydroxide ion (inset bottom). However, since the chain B active site contains partially-occupied atoms, all other Tyr34Phe MnSOD structures are five-coordinate, and the HERFD-XANES indicate five-coordinate complexes for Tyr34Phe MnSOD, this six-coordinate complex was not evaluated for mechanistic information. **c-d** Neutron structure of reduced Tyr34Phe MnSOD. For chain B, due to data quality issues, the nuclear density was difficult to interpret and density for WAT1 was not present. Since the HERFD-XANES data indicates that reduced Tyr34Phe MnSOD is five-coordinate like chain A, chain B was not used for mechanistic information. *Notably, this neutron structure is the lowest resolution, 2.5 Å of the three in Supplementary Table 6.* **e-f** Neutron structure of oxidized Tyr34Phe MnSOD. Green, orange, and magenta omit $|F_o| - |F_c|$ difference neutron scattering length density of protons displayed at 2.5 σ, 3.0σ, and 3.5 σ, respectively. Light blue $2|F_o| - |F_c|$ density is displayed at 1.0σ. Distances are in Å. Dashed lines indicate typical hydrogen bonds, and hashed lines indicate SSHBs, hydrogen bonds < 1.8 Å. D_2O_2-soaked and oxidized structures were solved to 2.3 Å resolution, while the reduced structure was solved to 2.5 Å resolution.

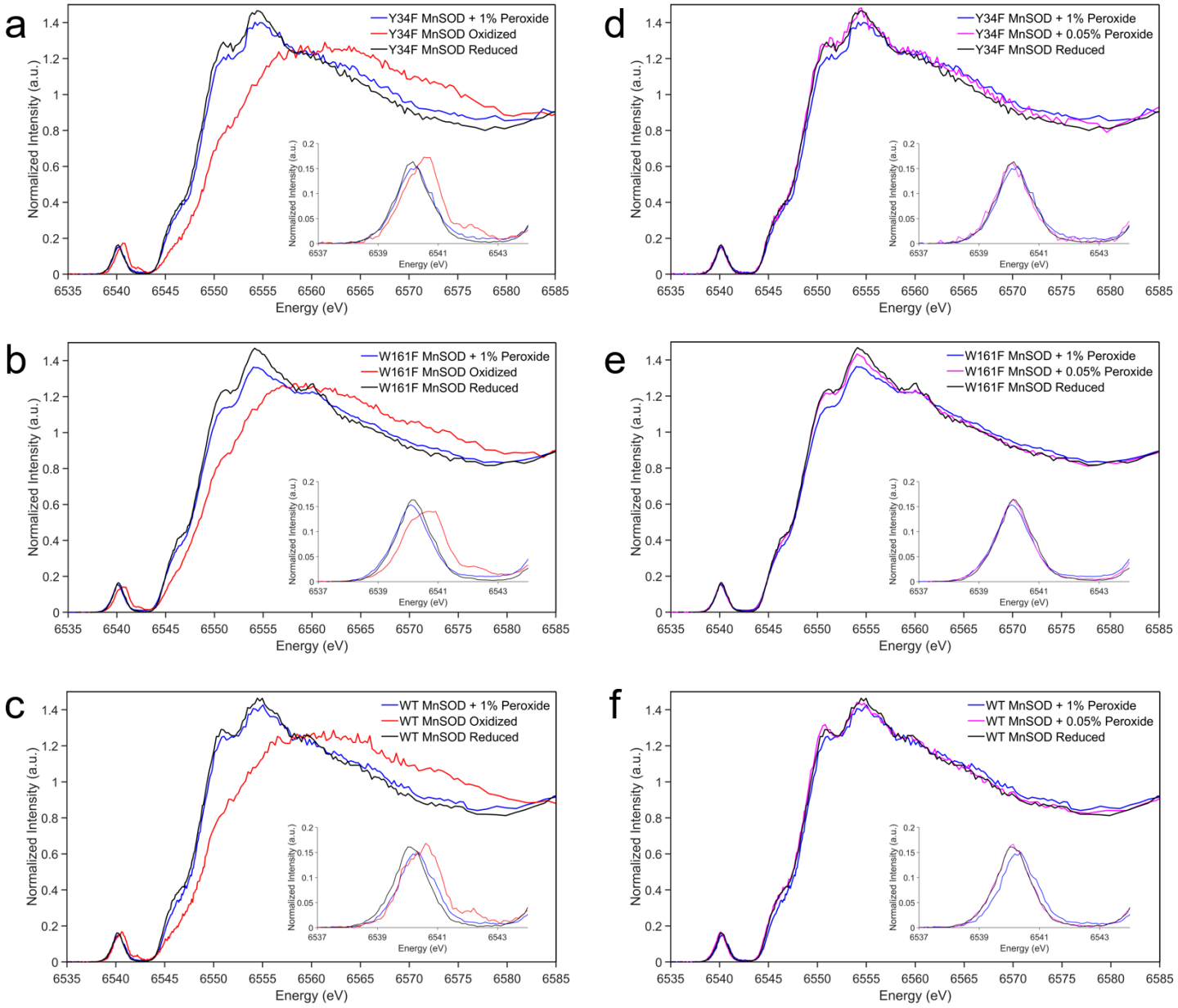

Supplementary Figure 2: Kα HERFD-XANES spectra of MnSOD. a-c HERFD-XANES of Tyr34Phe, Trp161Phe, and wildtype MnSOD in the 1% H_2O_2-soaked, oxidized, and reduced states. **d-f** HERFD-XANES of Tyr34Phe, Trp161Phe, and wildtype MnSOD in the 1% H_2O_2-soaked, 0.05% H_2O_2-soaked, and reduced states.

Supplementary Table 1. Individual steady-state rate constants of MnSOD.

MnSOD	k_1 (nM^{-1} s^{-1})	k_2 (nM^{-1} s^{-1})	k_3 (nM^{-1} s^{-1})	k_4 (s^{-1})
Human Wildtype[a]	1.5	1.1	1.1	120
Human Y34F[b]	0.55	<0.02	0.46	52
Human W161F[a]	0.30	<0.01	0.46	33
Human W123F[b]	0.76	<0.02	0.64	79

[a]pH 8.2 from Hearn *et al.* [1]

[b]pH 7.5 from Greenleaf *et al.* [2]

Supplementary Table 2. EXAFS fitting results for superoxide-soaked Tyr34Phe MnSOD.

Fit with Amino Acid Ligands and Dioxygen Species (5-coordinate)

Mn-O			Mn-N			Mn···C			Mn···C			Mn···O		
n	*r* (Å)	σ^2 x 10^3 (Å^2)	*n*	*r* (Å)	σ^2 x 10^3 (Å^2)	*n*	*r* (Å)	σ^2 x 10^3 (Å^2)	*n*	*r* (Å)	σ^2 x 10^3 (Å^2)	*n*	*r* (Å)	σ^2 x 10^3 (Å^2)
2	2.11	8.3	3	2.15	7.3	5	3.13	1.9	2	3.37	10	1	2.44	7.3
Mn···O···O			Mn···C···O			Mn···C···N			Mn···O···C···O					
n	*r* (Å)	σ^2 x 10^3 (Å^2)	*n*	*r* (Å)	σ^2 x 10^3 (Å^2)	*n*	*r* (Å)	σ^2 x 10^3 (Å^2)	*n*	*r* (Å)	σ^2 x 10^3 (Å^2)			
2	2.78	0.6	2	3.30	0	12	3.47	10	1	3.18	0			

χ^2	Reduced χ^2	R-Factor
41.79	10.20	0.0699

Fit with Amino Acids Ligands, Dioxygen Species, and Hypothetical Solvent Molecule (6-coordinate)

Mn-O			Mn-N			Mn···C			Mn···C			Mn···O		
n	*r* (Å)	σ^2 x 10^3 (Å^2)	*n*	*r* (Å)	σ^2 x 10^3 (Å^2)	*n*	*r* (Å)	σ^2 x 10^3 (Å^2)	*n*	*r* (Å)	σ^2 x 10^3 (Å^2)	*n*	*r* (Å)	σ^2 x 10^3 (Å^2)
3	2.11	8.3	3	2.15	7.3	5	3.13	1.9	2	3.37	10	1	2.44	7.3
Mn···O···O			Mn···C···O			Mn···C···N			Mn···O···C···O					
n	*r* (Å)	σ^2 x 10^3 (Å^2)	*n*	*r* (Å)	σ^2 x 10^3 (Å^2)	*n*	*r* (Å)	σ^2 x 10^3 (Å^2)	*n*	*r* (Å)	σ^2 x 10^3 (Å^2)			
2	2.78	0.6	2	3.30	0	12	3.47	10	1	3.18	0			

χ^2	Reduced χ^2	R-Factor
69.93	17.06	0.1170

Fit Only with Amino Acid Ligands (4-coordinate)

Mn-O			Mn-N			Mn···C			Mn···C			Mn···O		
n	*r* (Å)	σ^2 x 10^3 (Å^2)	*n*	*r* (Å)	σ^2 x 10^3 (Å^2)	*n*	*r* (Å)	σ^2 x 10^3 (Å^2)	*n*	*r* (Å)	σ^2 x 10^3 (Å^2)	*n*	*r* (Å)	σ^2 x 10^3 (Å^2)
1	2.11	8.3	3	2.15	7.3	5	3.13	1.9	2	3.37	10	-	-	-
Mn···O···O			Mn···C···O			Mn···C···N			Mn···O···C···O					
n	*r* (Å)	σ^2 x 10^3 (Å^2)	*n*	*r* (Å)	σ^2 x 10^3 (Å^2)	*n*	*r* (Å)	σ^2 x 10^3 (Å^2)	*n*	*r* (Å)	σ^2 x 10^3 (Å^2)			
-	-	-	2	3.30	0	12	3.47	10	1	3.18	0			

χ^2	Reduced χ^2	R-Factor
54.38	7.661	0.0910

Supplementary Table 3. EXAFS fitting results for peroxide-soaked Tyr34Phe MnSOD.

Fit with Amino Acid Ligands and Dioxygen Species (5-coordinate)

Mn-O			Mn-N			Mn···C			Mn···C			Mn···O		
n	*r* (Å)	σ^2 x 10^3 (Å^2)	*n*	*r* (Å)	σ^2 x 10^3 (Å^2)	*n*	*r* (Å)	σ^2 x 10^3 (Å^2)	*n*	*r* (Å)	σ^2 x 10^3 (Å^2)	*n*	*r* (Å)	σ^2 x 10^3 (Å^2)
2	2.11	8.3	3	2.15	7.3	5	3.13	1.9	2	3.37	10	1	2.44	7.3
Mn···O···O			Mn···C···O			Mn···C···N			Mn···O···C···O					
n	*r* (Å)	σ^2 x 10^3 (Å^2)	*n*	*r* (Å)	σ^2 x 10^3 (Å^2)	*n*	*r* (Å)	σ^2 x 10^3 (Å^2)	*n*	*r* (Å)	σ^2 x 10^3 (Å^2)			
2	2.78	0.6	2	3.30	0	12	3.47	10	1	3.18	0			

χ^2	Reduced χ^2	R-Factor
43.08	10.51	0.0522

Fit with Amino Acids Ligands, Dioxygen Species, and Hypothetical Solvent Molecule (6-coordinate)

Mn-O			Mn-N			Mn···C			Mn···C			Mn···O		
n	*r* (Å)	σ^2 x 10^3 (Å^2)	*n*	*r* (Å)	σ^2 x 10^3 (Å^2)	*n*	*r* (Å)	σ^2 x 10^3 (Å^2)	*n*	*r* (Å)	σ^2 x 10^3 (Å^2)	*n*	*r* (Å)	σ^2 x 10^3 (Å^2)
3	2.11	8.3	3	2.15	7.3	5	3.13	1.9	2	3.37	10	1	2.44	7.3
Mn···O···O			Mn···C···O			Mn···C···N			Mn···O···C···O					
n	*r* (Å)	σ^2 x 10^3 (Å^2)	*n*	*r* (Å)	σ^2 x 10^3 (Å^2)	*n*	*r* (Å)	σ^2 x 10^3 (Å^2)	*n*	*r* (Å)	σ^2 x 10^3 (Å^2)			
2	2.78	0.6	2	3.30	0	12	3.47	10	1	3.18	0			

χ^2	Reduced χ^2	R-Factor
98.32	23.99	0.1191

Fit Only with Amino Acid Ligands (4-coordinate)

Mn-O			Mn-N			Mn···C			Mn···C			Mn···O		
n	*r* (Å)	σ^2 x 10^3 (Å^2)	*n*	*r* (Å)	σ^2 x 10^3 (Å^2)	*n*	*r* (Å)	σ^2 x 10^3 (Å^2)	*n*	*r* (Å)	σ^2 x 10^3 (Å^2)	*n*	*r* (Å)	σ^2 x 10^3 (Å^2)
1	2.11	8.3	3	2.15	7.3	5	3.13	1.9	2	3.37	10	-	-	-
Mn···O···O			Mn···C···O			Mn···C···N			Mn···O···C···O					
n	*r* (Å)	σ^2 x 10^3 (Å^2)	*n*	*r* (Å)	σ^2 x 10^3 (Å^2)	*n*	*r* (Å)	σ^2 x 10^3 (Å^2)	*n*	*r* (Å)	σ^2 x 10^3 (Å^2)			
-	-	-	2	3.30	0	12	3.47	10	1	3.18	0			

χ^2	Reduced χ^2	R-Factor
62.15	8.755	0.0753

Supplementary Table 4. Active site Mn bond lengths of MnSOD neutron crystal structures.

Neutron	Tyr34Phe D_2O_2-Soaked[b]		Tyr34Phe Mn^{3+}SOD		Tyr34Phe Mn^{2+}SOD		Wildtype Mn^{3+}SOD		Wildtype Mn^{2+}SOD[c]	
PDB ID	9BVY		9BWM		9BW2		7KKS		7KKW	
Mn Bonds (Å)	A	B	A	B	A	B	A	B	A	B
Mn-$N^{\varepsilon 2}$(H26)	2.17	2.10	2.13	2.14	2.10	2.07	2.07	2.07	2.26	2.10
Mn-$N^{\varepsilon 2}$(H74)	2.23	2.18	2.22	2.16	2.11	2.11	2.13	2.12	2.19	2.25
Mn-$O^{\varepsilon 2}$(D159)	2.13	2.03	2.11	2.11	2.15	2.16	1.95	1.94	2.44	2.15
Mn-$N^{\varepsilon 2}$(H163)	2.21	2.19	2.22	2.22	2.13	2.13	2.06	2.14	2.23	2.21
Mn-O(WAT1)	-	1.76	2.20	-	1.95	1.93	1.78	1.76	2.12	2.22
Mn-O^1(LIG)[a]	2.00	-	-	-	-	-	-	-	-	-
Mn-O^2(LIG)	2.34	-	-	-	-	-	-	-	-	-
Mn-O(OL)	-	1.80	-	-	-	-	-	-	1.82	-

Neutron	Trp161Phe D_2O_2-Soaked[d]		Trp161Phe Mn^{3+}SOD		Trp161Phe Mn^{2+}SOD	
PDB ID	8VHW		8VJ0		8VHY	
Mn Bonds (Å)	A	B	A	B	A	B
Mn-$N^{\varepsilon 2}$(H26)	2.13	2.20	2.01	2.01	2.20	2.11
Mn-$N^{\varepsilon 2}$(H74)	2.13	2.28	2.15	2.15	2.19	2.16
Mn-$O^{\varepsilon 2}$(D159)	2.20	2.05	2.01	2.01	2.13	2.20
Mn-$N^{\varepsilon 2}$(H163)	2.25	2.17	2.15	2.15	2.14	2.15
Mn-O(WAT1)	2.13	-	1.84	1.84	2.37	2.24
Mn-O^1(LIG)[a]	-	1.94	-	-	-	-
Mn-O^2(LIG)	-	2.61	-	-	-	-
Mn-O(OL)	-	-	-	-	-	-

[a]O^1(LIG) refers to the closest oxygen atom of the dioxygen species.

[b]Only chain A of D_2O_2-soaked Tyr34Phe MnSOD is bound by a dioxygen species, denoted as LIG. For chain A, an $^-$OD molecule (denoted OL for oxygen ligand) is observed binding opposite of Asp159 and is six-coordinate. Note that HERFD-XANES (**Supplementary Fig. 2a**) and EXAFS suggest a five-coordinate complex (**Supplementary Table 2**).

[c]For chain A of wildtype Mn^{2+}SOD, an $^-$OD molecule is observed binding opposite of Asp159 and is six-coordinate. Chain B is in the typical five-coordinated state. Note that HERFD-XANES suggest a five-coordinate complex (**Supplementary Fig. 2c**).

[d]Only chain B of D_2O_2-soaked Trp161Phe MnSOD is bound by a dioxygen species.

Supplementary Table 5. Active site Mn bond lengths of DFT-optimized structures.

Wildtype Mn^{3+}SOD (S=2)		Tyr34Phe Mn^{3+}SOD (S=2)	
Bond	DFT (Å)	Bond	DFT (Å)
Mn-$N^{\varepsilon 2}$(H26)	2.06	Mn-$N^{\varepsilon 2}$(H26)	2.04
Mn-$N^{\varepsilon 2}$(H74)	2.13	Mn-$N^{\varepsilon 2}$(H74)	2.11
Mn-$N^{\varepsilon 2}$(H163)	2.06	Mn-$N^{\varepsilon 2}$(H163)	2.09
Mn-$O^{\delta 2}$(D159)	1.95	Mn-$O^{\delta 2}$(D159)	1.98
Mn-O(WAT1)	1.80	Mn-O(WAT1)	1.82
Wildtype Mn^{2+}SOD (S=5/2)		Tyr34Phe Mn^{2+}SOD (S=5/2)	
Bond	DFT (Å)	Bond	DFT (Å)
Mn-$N^{\varepsilon 2}$(H26)	2.23	Mn-$N^{\varepsilon 2}$(H26)	2.22
Mn-$N^{\varepsilon 2}$(H74)	2.18	Mn-$N^{\varepsilon 2}$(H74)	2.18
Mn-$N^{\varepsilon 2}$(H163)	2.19	Mn-$N^{\varepsilon 2}$(H163)	2.19
Mn-$O^{\delta 2}$(D159)	2.06	Mn-$O^{\delta 2}$(D159)	2.06
Mn-O(WAT1)	2.14	Mn-O(WAT1)	2.13
Trp161Phe Mn^{2+}SOD + HO_2^- (S=5/2)		Tyr34Phe Mn^{2+}SOD + HO_2^- (S=5/2)	
Bond	DFT (Å)	Bond	DFT (Å)
Mn-$N^{\varepsilon 2}$(H26)	2.24	Mn-$N^{\varepsilon 2}$(H26)	2.28
Mn-$N^{\varepsilon 2}$(H74)	2.16	Mn-$N^{\varepsilon 2}$(H74)	2.20
Mn-$N^{\varepsilon 2}$(H163)	2.15	Mn-$N^{\varepsilon 2}$(H163)	2.16
Mn-$O^{\delta 2}$(D159)	2.06	Mn-$O^{\delta 2}$(D159)	2.17
Mn-O(PEO)	2.08	Mn-O(PEO)	2.10
Tyr34Phe Mn^{3+}SOD + HO_2^- (S=2)		Tyr34Phe Mn^{2+}SOD + $HO_2^{\bullet}$ (S=3)	
Bond	DFT (Å)	Bond	DFT (Å)
Mn-$N^{\varepsilon 2}$(H26)	2.00	Mn-$N^{\varepsilon 2}$(H26)	2.12
Mn-$N^{\varepsilon 2}$(H74)	2.07	Mn-$N^{\varepsilon 2}$(H74)	2.16
Mn-$N^{\varepsilon 2}$(H163)	2.19	Mn-$N^{\varepsilon 2}$(H163)	2.17
Mn-$O^{\delta 2}$(D159)	2.01	Mn-$O^{\delta 2}$(D159)	2.01
Mn-O(PEO)	1.82	Mn-O(SUP)	2.37

Supplementary Table 6. Data collection and refinement statistics for Tyr34Phe MnSOD.

Data Collection Statistics					
	Neutron			X-ray	
Variant	Tyr34Phe MnSOD				
Chemical State	D_2O_2-Soaked	Reduced	Oxidized	H_2O_2-Soaked	Reduced
PDB Code	9BVY	9BW2	9BWM	9BWQ	9BWR
Growth Conditions	Microgravity			Earth	
Diffraction Source	MaNDi			SSRL Beamline 14-1	Rigaku FR-E SuperBright
Temperature (K)	100	296	296	100	100
Space group	$P6_122$			$P6_122$	
a, *b*, *c* (Å)	78.69. 78.69, 239.94	79.4, 79.4, 238.43	79.29, 79.29, 240.61	78.22, 78.22, 239.50	78.09, 78.09, 235.19
α, β, γ (°)	90, 90, 120			90, 90, 120	
Wavelengths (Å)	2-4			0.9795	1.5418
No. of images	11	10	13	625	386
Exposure time	36 h	28 h	35 h	1 s	300 s
No. of unique reflections	18698	14940	20703	85139	65175
Total No. of reflections	73477	123482	161187	170167	526729
Resolution range (Å)	14.84-2.30 (2.37-2.30)	14.55-2.50 (2.58-2.5)	14.39-2.28 (2.36-2.28)	39.13-1.40 (1.45-1.40)	50.00-1.50 (1.53-1.50)
Multiplicity	4.1 (3.4)	8.3 (6.7)	7.79 (6.15)	13.5 (13.6)	8.1 (5.8)
I/σ(I)	5.1 (2.7)	6.6 (3.8)	7.4 (3.7)	7.3 (1.6)	7.5 (1.38)
R_{merge}	0.277 (0.266)	0.321 (0.292)	0.246 (0.323)	-	-
R_{meas}	0.310 (0.305)	0.340 (0.315)	0.263 (0.349)	0.039 (0.458)	0.299 (0.816)
$CC_{1/2}$	0.783 (0.259)	0.766 (0.117)	0.953 (0.476)	0.999 (0.788)	0.847 (0.578)
R_{pim}	0.133 (0.142)	0.106 (0.112)	0.090 (0.127)	0.027 (0.324)	0.089 (0.411)
Completeness (%)	90.4 (75.3)	91.3 (90.7)	97.78 (88.40)	98.8 (97.5)	94.4 (85.2)
Refinement Statistics					
R_{work}	0.265	0.293	0.242	0.184	0.189
R_{free}	0.299	0.330	0.275	0.205	0.210
[a]No. of atoms					
Protein	6547	6233	6617	3160	3160
[b]Solvent	1068	496	147	571	782
Mn	2	2	2	2	2
R.m.s. deviations					
Bond lengths (Å)	0.002	0.006	0.001	0.004	0.003
Bond angles (°)	0.541	0.522	0.505	0.683	0.638
Average *B*-factor	3.69	15.36	35.45	19.65	18.38
Protein	3.73	15.45	35.42	18.42	15.41
Water	3.45	13.87	36.74	25.90	30.07
Mn	2.38	14.70	42.91	14.21	9.99
Peroxide	2.98	-	-	16.82	-
[c]Coordinate Error (Å)	0.30	0.42	0.30	0.15	0.15

[a]No. of atoms is inclusive of H/D atoms for neutron structures.

[b]The neutron structure of reduced and oxidized Tyr34Phe were collected at room temperature and, as a result, have fewer solvent atoms compared to the other structures.

[c]Estimated coordinate error determined by PHENIX. Note that the disorder of atom positions is reflected by the *B*-factor.

Evaluation of HERFD-XANES data: Retention of the product-inhibited complex is dependent on the Gln143 position.

As the XAS and neutron crystallographic data of Tyr34Phe MnSOD demonstrated the formation of a five-coordinated Mn^{2+}SOD with a singly-protonated dioxygen species replacing the WAT1 position, we wondered if the formation and retention of the inhibited complex could be distinguished with other variants of MnSOD. In the context of Tyr34Phe MnSOD, we also sought to define whether the enrichment of product inhibition was due to the loss of the ionizable Tyr group only or also due to the perturbation of the Gln143-WAT1 SSHB interaction. For example, the Trp161Phe MnSOD variant alters a residue directly adjacent to Gln143 and has enriched product-inhibition kinetics like those of Tyr34Phe MnSOD (**Supplementary Table 1**)[3]. For wildtype, Tyr34Phe, and Trp161Phe, we performed XANES in the HERFD mode of detection, which allows a large improvement in energy resolution and sensitivity compared to conventional XANES[4-6]. Here, we focused on comparing the reduced form of the variants to those of peroxide-soaked counterparts. As all these complexes are expected to be five-coordinated d^5 with spin S=5/2, we sought to distinguish fine details of the spectra offered by the HERFD mode of detection.

For HERFD-XANES data of Tyr34Phe MnSOD, the features of the reduced and peroxide-soaked forms seen in conventional XANES (**Fig. 2a**) are also observed. While both forms have similar rising edge energies to indicate the same oxidation state of the Mn ion, the peroxide-soaked form is seen with a lower intensity at ~6550-6555 eV and a higher intensity at ~6565-6580 eV (**Supplementary Fig. 3a**). Unique to the HERFD data is the observation of a higher intensity shoulder of peroxide-soaked Tyr34Phe MnSOD at ~6565 eV and the ability to better resolve the pre-edge peaks for both samples. The peak centers of the pre-edge are within ~0.2 eV of each other, while greater intensity for the higher energy tail (~6542.5 eV) is distinguishable for peroxide-soaked Tyr34Phe MnSOD. Overall, reduced and peroxide-soaked Tyr34Phe MnSOD spectra have distinct features between each other, and the general shape trends are reproducible both with conventional XANES (**Fig. 2a**) and HERFD-XANES (**Supplementary Fig. 3a**) and suggest two differing five-coordinate Mn^{2+} complexes are measured.

Trp161Phe MnSOD, like Tyr34Phe MnSOD, exhibits kinetics indicating a highly product-inhibited enzyme ($k_3 >> k_2$, **Supplementary Table 1**). HERFD-XANES data of reduced and peroxide-soaked Trp161Phe MnSOD demonstrates the same trends as Tyr34Phe MnSOD, with a lower intensity at ~6550 eV and a higher intensity at ~6562-6570 eV (**Supplementary Fig. 3b**). Likewise, a lower intensity for the pre-edge maxima at ~6540 eV and a greater intensity for the pre-edge tail at ~6542.5 eV is seen for peroxide-soaked Trp161Phe MnSOD compared to the reduced counterpart. Overall, similar trends are observed between reduced and peroxide-soaked forms of Tyr34Phe and Trp161Phe MnSOD.

Next, we wondered how well the product-inhibited complex could be cryotrapped in wildtype MnSOD, where $k_3 = k_2$ (**Supplementary Table 1**). Compared to Tyr34Phe and Trp161Phe, wildtype has the least noticeable difference in intensity among the 6550-6560 eV region between its peroxide-soaked and reduced counterparts (**Supplementary Fig. 3c**). However, a higher intensity at ~6570 eV is still observed for peroxide-soaked wildtype as well as the higher intensity for the pre-edge at ~6542.5 eV. Of the reduced and peroxide-soaked pairs, the spectra of the wildtype pair are the most similar in their overall shape. Since the wildtype enzyme exhibits physiological product inhibition levels ($k_3 = k_2$, **Supplementary Table 1**) compared to the Tyr34Phe and Trp161Phe variants that are enriched for product inhibition ($k_3 >> k_2$ and lower k_4 compared to wildtype, **Supplementary Table 1**), a potential explanation for the less pronounced differences for the wildtype pair is that the peroxide-soaked data may reflect a mixture of species rather than a fully isolated product-bound complex.

When comparing the HERFD-XANES data of wildtype, Tyr34Phe, and Trp161Phe peroxide-soaked MnSOD variants, several commonalities and trends are observed. First, the edge of the three samples lay on top of each other (**Supplementary Fig. 3d**), indicating that the oxidation and spin state is maintained across the variants. For the pre-edge, the apex of the pre-edge intensity for the peroxide-soaked samples is found to be consistently lower than the reduced counterparts in addition to an increase in the intensity of the high-energy pre-edge tail (inset, **Supplementary Fig. 3a-d**). While the apex peak of the pre-edge shifts within 0.2 eV among the samples tested (inset, **Supplementary Fig. 3d**), the significance of the shift is unclear due to the closeness of the peaks. For the overall spectral shape, peroxide-soaked Trp161Phe MnSOD has the most drastic shift compared to its reduced counterpart (6550-6580 eV, **Supplementary Fig. 3b**). Furthermore, peroxide-soaked Trp161Phe MnSOD also has the lowest intensity at the 6550 eV region compared to other peroxide-soaked variants (**Supplementary Fig. 3d**). This may be because Trp161Phe MnSOD is the most product-inhibited of the three MnSOD forms tested, ($k_3 >> k_2$ and lowest k_4, **Supplementary Table 1**). Wildtype is the least product-inhibited when compared to Trp161Phe and Tyr34Phe, ($k_3 = k_2$ and higher k_4, **Supplementary Table 1**) and has the least drastic shape shift between its reduced and peroxide-soaked counterparts. Tyr34Phe, while still highly product-inhibited ($k_3 >> k_2$), has a k_4 value between that of Trp161Phe and wildtype and may explain why the 6550 eV intensity is intermediate (**Supplementary Fig. 3d**). While previous kinetic models ascribe k_4 as the zero-order decay of the inhibited complex to a trivalent Mn ion[1,3,7-9], some studies have indicated that the product-inhibited complex decays to divalent Mn ion[3,10]. Indeed, exposing our samples to lesser amounts of peroxide before HERFD-XANES data collection leads to spectra that more closely resemble reduced spectra (**Supplementary Fig. 2**). These observations indicate that retention of the inhibited complex is not exclusively dependent on a proton transfer from Tyr34 but instead on other factors of the active site.

To provide insight into the mechanism of product inhibition, we compared our D_2O_2-soaked Tyr34Phe MnSOD neutron structure with that of our previous D_2O_2-soaked Trp161Phe MnSOD neutron structure (**Supplementary Fig. 3e,** PDB ID 8VHW). The orientation of the singly-protonated dioxygen ligand differs between the two structures. The O^1-O^2(LIG) axis for Trp161Phe is nearly coaxial with that of the Mn-Asp159 bond. For Tyr34Phe, the O^1-O^2(LIG) axis is at an angle of ~55° to the Mn-Asp159 bond. These orientation differences are most likely attributed to the residue at position 161. LIG closely interacts with Trp161 in Tyr34Phe MnSOD (**Fig. 3a**), and when this contact is absent, LIG can assume a different orientation. Interestingly, the strong LIG-Gln143 hydrogen bond in Trp161Phe MnSOD coincides with a longer retention of the product inhibited-complex (k_4, **Supplementary Table 1**). However, since the 161 position is occupied by a tryptophan residue in wildtype, the LIG orientation in Tyr34Phe MnSOD is probably close to what would occur physiologically.

Both Tyr34Phe and Trp161Phe MnSOD have nearly ablated catalysis for the Mn^{2+} to Mn^{3+} redox reaction (k_2, **Supplementary Table 1**) and therefore proceed predominately through the product-inhibited pathway (k_3 and k_4, **Supplementary Table1**). To investigate whether deficient k_2 catalysis in Tyr34Phe is from a loss of the Tyr34 ionizable group or the distortion of the Gln143 position, we compared the neutron structure of Tyr34Phe Mn^{2+}SOD with our previous Trp161Phe Mn^{2+}SOD structure that preserves the number of ionizable groups (**Supplementary Fig. 3f,** PDB ID 8VHY). Both variant structures have a lengthened WAT1-Gln143 interaction compared to wildtype which is a site of proton transfer (**Fig. 1b**)[11]. This suggests that the k_2 PCET reaction is not solely dependent on the ionization of Tyr34 but also on tight WAT1-Gln143 hydrogen bonding. Furthermore, the weakened interaction for the variants allows WAT1 to be more easily displaced by dioxygen species for the formation of the product-inhibited complex through k_3 (**Supplementary Table 1**). Altogether, both the Tyr34Phe and Trp161Phe Mn^{2+}SOD structures highlight the importance of the WAT1-Gln143 interaction for catalysis.

Previous studies have indicated that relief of inhibited complex (i.e., disassociation of the dioxygen species from the Mn ion) is proton transfer dependent, with Tyr34 being the most obvious proton donor[7,8]. Indeed, mutation of Tyr34 to phenylalanine leads to a slower disassociation of the inhibited complex (k_4, **Supplementary Table 1**). However, several other point mutations lead to the same effect, including Trp161Phe and Trp123Phe[7,8]. What these variants have in common with Tyr34Phe is that the affected residue position is directly adjacent to Gln143, which has been shown to change protonation states (**Fig. 1b**)[11]. From the D_2O_2-soaked neutron structure of Trp161Phe MnSOD, we previously postulated that the strong interaction between LIG and Gln143 could represent a possible proton transfer site (**Supplementary Fig. 3e**)[12]. However, this suggestion is at odds with the Tyr34Phe counterpart, which has a weak hydrogen bonding interaction with the already protonated O^2(LIG) atom and a faster Mn-dioxo dissociation (k_4, **Supplementary Table 1**). This means

Gln143 may not directly protonate LIG and that a stronger LIG-Gln143 interaction instead contributes to longer retention of the inhibited complex. An alternative proton donor for the protonation of LIG to form H_2O_2 could be a solvent molecule. Proton donation from a solvent molecule would have to compete with the LIG-Gln143 interaction, and this also explains why a short LIG-Gln143 hydrogen correlates with longer retention of the inhibited complex. Overall, our analysis of D_2O_2-soaked MnSOD variants suggests that Gln143 plays a role in the retention of the inhibited complex.

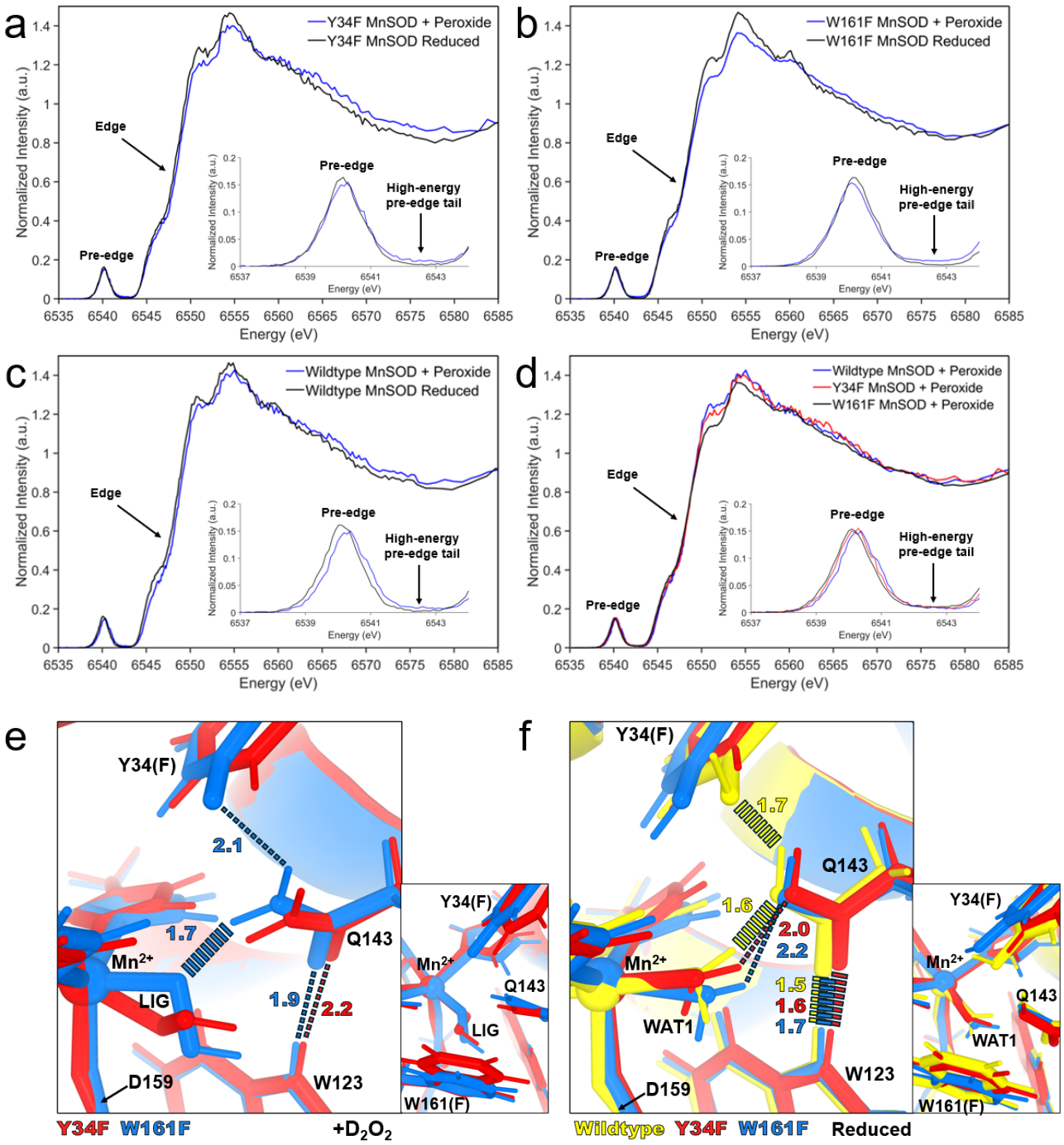

Supplementary Figure 3: HERFD-XANES and neutron structures of Tyr34Phe, Trp161Phe, and wildtype MnSOD. a HERFD-XANES spectra of H_2O_2-soaked and reduced Tyr34Phe MnSOD. **b** HERFD-XANES spectra of H_2O_2-soaked and reduced Trp161Phe MnSOD. **c** HERFD-XANES spectra of H_2O_2-soaked and reduced wildtype MnSOD. **d** HERFD-XANES spectra of H_2O_2-soaked wildtype MnSOD, H_2O_2-soaked Tyr34Phe MnSOD, and H_2O_2-soaked Trp161Phe MnSOD. **e** Active site overlay of D_2O_2-soaked Tyr34Phe MnSOD (this study) and D_2O_2-soaked Trp161Phe MnSOD (PDB ID 8VHW, solved at 2.3 Å resolution). **f**

Active site overlay of wildtype Mn^{2+}SOD (PDB ID 7KKW, solved at 2.3 Å resolution), Tyr34Phe Mn^{2+}SOD (this study, solved at 2.5 Å resolution), and Trp161Phe Mn^{2+}SOD (PDB ID 8VHY, solved at 2.3 Å resolution). For **e-f**, dashed lines indicate hydrogen bonds ≥ 1.8 Å, and hashed lines indicate SSHBs that are hydrogen bonds < 1.8 Å.

Evaluation of XAS pre-edge: The electronic configuration of the Mn ion.

For enzymes that use metal centers to catalyze redox reactions, the arrangement of the metal 3d orbitals determines how electrons are exchanged and how substrates orient for catalysis[13]. For MnSOD, the metal ion is in a distorted C_{3v} symmetry environment with either 4 or 5 occupied electrons in the α-manifold, depending on the oxidation state of the metal[14]. For Mn^{3+} with S = 2, the e_π (xz/yz) and e_σ (xy/x^2-y^2) α orbitals are occupied, while Mn^{2+} with S = 5/2 also has the z^2 α orbital occupied (**Supplementary Fig. 4a**). The z^2 α orbital exchanges electrons during redox reactions as it is the lowest unoccupied molecular orbital (LUMO) for Mn^{3+} and the highest occupied molecular orbital (HOMO) for Mn^{2+}. This means that mono- or dioxygen species are most likely to bind the Mn ion along the z-axis for reactivity (**Supplementary Fig. 4b**). For further insight into the MnSOD metal 3d orbitals, we compared the K-pre-edge spectra found through time-dependent DFT (TD-DFT) simulations with spectra measured from HERFD-XANES.

In K-edge XAS, the pre-edge corresponds to 1s to 3d transitions that gain intensity through 4p character mixing into the 3d orbitals from symmetry distortions and/or loss of inversion symmetry[15-17]. The contribution of the 4p electric dipole is about one hundred times stronger than the 3d quadrupole contributions, so a small amount of 4p mixing can significantly influence the pre-edge spectra[15,16,18]. With TD-DFT simulations, the 3d/4p contributions can be assigned to the experimental pre-edge spectra (**Supplementary Fig. 4c-h**). In the plots, the vertical stick heights represent the intensity of 1s to 3d/4p transitions from quadrupole and dipole contributions, and percentage of 3d and 4p character from ground-state DFT are listed. To identify the impact of the Tyr34Phe variant on the electronic configuration of the metal, we compared its Mn^{3+}SOD, Mn^{2+}SOD, and H_2O_2-soaked pre-edge spectra to those of wildtype and Trp161Phe.

The experimental pre-edge spectra are similar between wildtype and Tyr34Phe Mn^{3+}SOD, indicating that the Tyr34Phe variant does not significantly alter the Mn^{3+} ion orbital configuration (**Supplementary Fig. 4c, d**). The TD-DFT spectra are also similar between the two complexes, though the simulated spectra underestimate the splitting of orbital transitions and overestimates intensity. This misestimation has been previously reported for other transition metal complexes of similar symmetry[18,19]. In brief, TD-DFT overestimates the exchange interaction between the 1s core hole and the valence 3d orbitals, which results in decreased energy splitting between transitions. Regardless, the e_σ orbitals are the primary contributors to the intensities of the pre-edge as they have significant dipole character from 4p mixing. Indeed, ground-state DFT indicates that the e_σ β orbitals have 1.5-1.6% 4p character and have the highest 4p mixing compared to the other 3d orbitals (inset table, **Supplementary Fig. 4c, d**). In the experimental spectra, a high-energy tail is observed at ~6542.5 eV, which is likely to be the z^2 β transition as indicated by TD-DFT. Assignment of the lower energy z^2 α and e_π β transitions in the experimental spectra is less clear, but they may contribute to the left shoulders of

the pre-edge peaks. Despite the misestimation of the energy splitting with TD-DFT, the contributions of the e_σ and z^2 β transitions can be assigned to the experimental spectra.

For wildtype and Tyr34Phe Mn^{2+}SOD, the experimental pre-edge spectra are nearly identical (**Supplementary Fig. 4e, f**). DFT calculations suggest that the e_σ β orbitals contribute the majority of the intensity to the pre-edge for both wildtype and Tyr34Phe Mn^{2+}SOD due to 4p mixing. The z^2 β transitions found at higher energies are of pure quadrupole character that contributes weak intensity. At lower energy, the e_π β transitions likely contribute weak intensity to the left shoulders of the pre-edge peaks. For the resting state Mn^{2+}SOD complexes, the experimental and simulated spectra agree with each other and allow the assignment of all the orbital transitions.

The H_2O_2-soaked Trp161Phe and Tyr34Phe complexes have similar experimental spectra though the calculated spectra suggest differences in orbital transitions (**Supplementary Fig. 4g, h**). The calculated spectra used a Mn^{2+} ion along with a HO_2^- as the dioxygen species. For Trp161Phe, the e_σ and e_π β transitions are close in energy and suggest further distortions of C_{3v} symmetry and mixing of the d orbitals (**Supplementary Fig. 4g**). These e transitions are mostly of dipole character, with the e_σ set bearing the most. The z^2 β orbital is the highest energy transition with weak intensity. For Tyr34Phe, the d orbitals also mix, and the e_σ transitions begin to split (**Supplementary Fig. 4h**). Between Tyr34Phe and Trp161Phe, the energy of the z^2 β transition differs, with that of Trp161Phe being ~0.4 eV higher than Tyr34Phe (**Supplementary Fig. 4g, h**). This is reflective of different Mn ion interactions along the z-axis, like with HO_2^-. However, the calculated intensities of the z^2 β transitions are weak, and the energies that these transitions occur in the experimental spectra are not obvious. Overall, the pre-edge spectral shapes of H_2O_2-soaked Trp161Phe and Tyr34Phe complexes are similar, though they have different transition energies.

Analysis of the K-pre-edge for various MnSOD complexes indicates that the hydroxyl group of Tyr34 does not significantly affect the metal 3d transitions of the Mn^{3+}SOD and Mn^{2+}SOD resting states (**Supplementary Fig. 4c-f**). The pre-edge spectra for wildtype and Tyr34Phe resting states are dominated by e_σ transitions that are flanked by weaker intensity e_π and z^2 transitions. The majority of the intensities from the e_σ orbitals are from dipole contributions as a result of 4p mixing. Specifically, the metal $4p_x$ and $4p_y$ mix with the $3d_{x^2-y^2}$ and $3d_{xy}$ orbitals. These orbitals have σ-overlap with the Mn ligands along the xy plane, namely with residues His74, His163, and Asp159 (**Supplementary Fig. 4b)**. The deviation of these trigonal ligands away from idealized 120° angles in C_{3v} symmetry results in 4p mixing and significant intensity contributions to the pre-edge peak[18].

The TD-DFT calculations for the Trp161Phe and Tyr34Phe Mn^{2+}SOD that are bound by HO_2^- have similar spectral shapes though different energies of for the e_σ and z^2 transitions (**Supplementary Fig. 4g, h**). This may, in part, be explained by the different orientations of HO_2^- bound to the Mn^{2+} ion that leads to

different orbital characteristics (**Supplementary Fig. 3e**). The orbital transitions for these complexes have strong covalent mixing with the Mn-bound ligands, leading to less overall d character compared to the resting state complexes. The d orbitals also mix with each other and suggest the complexes are further distorting away from C_{3v} symmetry (**Supplementary Fig. 4g, h**). TD-DFT analysis of dioxygen-bound Trp161Phe and Tyr34Phe Mn^{2+}SOD suggest that different modes of HO_2^- binding may result in similar spectra.

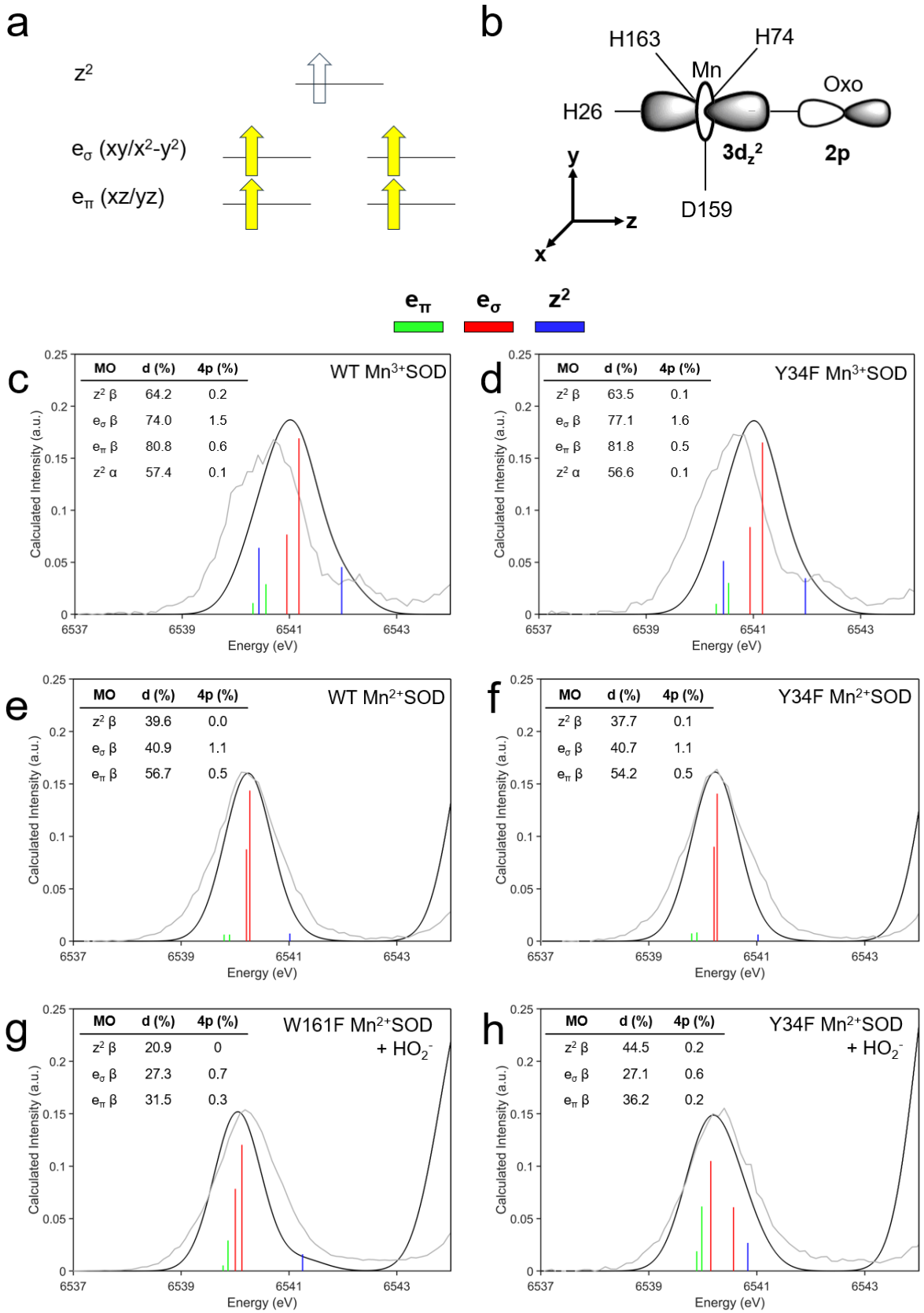

Supplementary Figure 4: MnSOD metal 3d orbital transitions. a Schematic molecular orbital diagram of high spin Mn^{3+} and Mn^{2+} complexes. The e_σ and e_π orbitals of the α-manifold are occupied for Mn^{3+}, while Mn^{2+} also has the z^2 α orbital occupied. The z^2 α orbital exchanges electrons during catalysis. **b** Schematic of

the Mn ion in an idealized C_{3v} environment highlighting the interaction of the Mn ion $3d_z^2$ orbital with the 2p orbital of a mono- or dioxygen species. **c-h** Comparison of experimental MnSOD K-pre-edge spectra with TD-DFT simulated intensities. The metal 3d orbital transitions are colored by vertical lines: e_π in green, e_σ in red, and z^2 in blue. The tables within the panels list the percentage 3d and 4p molecular orbital character found from ground-state DFT and Löwdin analysis. Bond distances of DFT-optimized structures are found in **Supplementary Table 5**.

Supplementary References.

1. Hearn, A. S., Stroupe, M. E., Cabelli, D. E., Lepock, J. R., Tainer, J. A., Nick, H. S. & Silverman, D. N. "Kinetic analysis of product inhibition in human manganese superoxide dismutase" *Biochemistry*, **40**, 12051-12058 (2001).
2. Greenleaf, W. B., Perry, J. J., Hearn, A. S., Cabelli, D. E., Lepock, J. R., Stroupe, M. E., Tainer, J. A., Nick, H. S. & Silverman, D. N. "Role of hydrogen bonding in the active site of human manganese superoxide dismutase" *Biochemistry*, **43**, 7038-7045 (2004).
3. Cabelli, D. E., Guan, Y., Leveque, V., Hearn, A. S., Tainer, J. A., Nick, H. S. & Silverman, D. N. "Role of tryptophan 161 in catalysis by human manganese superoxide dismutase" *Biochemistry*, **38**, 11686-11692 (1999).
4. Hamalainen, K., Siddons, D. P., Hastings, J. B. & Berman, L. E. "Elimination of the inner-shell lifetime broadening in x-ray-absorption spectroscopy" *Phys Rev Lett*, **67**, 2850-2853 (1991).
5. de Groot, F. M. F., Krisch, M. H. & Vogel, J. "Spectral sharpening of the Pt L edges by high-resolution x-ray emission" *Phys. Rev. B*, **66** (2002).
6. Kroll, T., Hadt, R. G., Wilson, S. A., Lundberg, M., Yan, J. J., Weng, T. C., Sokaras, D., Alonso-Mori, R., Casa, D., Upton, M. H., Hedman, B., Hodgson, K. O. & Solomon, E. I. "Resonant inelastic X-ray scattering on ferrous and ferric bis-imidazole porphyrin and cytochrome c: nature and role of the axial methionine-Fe bond" *J Am Chem Soc*, **136**, 18087-18099 (2014).
7. Abreu, I. A. & Cabelli, D. E. "Superoxide dismutases-a review of the metal-associated mechanistic variations" *Biochim Biophys Acta*, **1804**, 263-274 (2010).
8. Sheng, Y., Abreu, I. A., Cabelli, D. E., Maroney, M. J., Miller, A. F., Teixeira, M. & Valentine, J. S. "Superoxide dismutases and superoxide reductases" *Chem Rev*, **114**, 3854-3918 (2014).
9. Hearn, A. S., Stroupe, M. E., Cabelli, D. E., Ramilo, C. A., Luba, J. P., Tainer, J. A., Nick, H. S. & Silverman, D. N. "Catalytic and structural effects of amino acid substitution at histidine 30 in human manganese superoxide dismutase: insertion of valine C gamma into the substrate access channel" *Biochemistry*, **42**, 2781-2789 (2003).
10. Hearn, A. S., Tu, C., Nick, H. S. & Silverman, D. N. "Characterization of the product-inhibited complex in catalysis by human manganese superoxide dismutase" *J Biol Chem*, **274**, 24457-24460 (1999).
11. Azadmanesh, J., Lutz, W. E., Coates, L., Weiss, K. L. & Borgstahl, G. E. O. "Direct detection of coupled proton and electron transfers in human manganese superoxide dismutase" *Nat Commun*, **12**, 2079 (2021).
12. Azadmanesh, J., Slobodnik, K., Struble, L. R., Lutz, W. E., Coates, L., Weiss, K. L., Myles, D. A. A., Kroll, T. & Borgstahl, G. E. O. "Revealing the atomic and electronic mechanism of human manganese superoxide dismutase product inhibition" *Nat Commun*, **15**, 5973 (2024).
13. Solomon, E. I. "Preface forum: "functional insight from physical methods on metalloenzymes"" *Inorg Chem*, **44**, 723-726 (2005).
14. Vance, C. K. & Miller, A. F. "Novel insights into the basis for Escherichia coli superoxide dismutase's metal ion specificity from Mn-substituted FeSOD and its very high E(m)" *Biochemistry*, **40**, 13079-13087 (2001).
15. Leto, D. F. & Jackson, T. A. "Mn K-edge X-ray absorption studies of oxo- and hydroxo-manganese(IV) complexes: experimental and theoretical insights into pre-edge properties" *Inorg Chem*, **53**, 6179-6194 (2014).
16. Westre, T. E., Kennepohl, P., DeWitt, J. G., Hedman, B., Hodgson, K. O. & Solomon, E. I. "A Multiplet Analysis of Fe K-Edge 1s → 3d Pre-Edge Features of Iron Complexes" *J. Am. Chem. Soc.*, **119**, 6293-6314 (1997).
17. Kroll, T., Baker, M. L., Wilson, S. A., Lundberg, M., Juhin, A., Arrio, M. A., Yan, J. J., Gee, L. B., Braun, A., Weng, T. C., Sokaras, D., Hedman, B., Hodgson, K. O. & Solomon, E. I. "Effect of 3d/4p Mixing on 1s2p Resonant Inelastic X-ray Scattering: Electronic Structure of Oxo-Bridged Iron Dimers" *J Am Chem Soc*, **143**, 4569-4584 (2021).

18. Braun, A., Gee, L. B., Mara, M. W., Hill, E. A., Kroll, T., Nordlund, D., Sokaras, D., Glatzel, P., Hedman, B., Hodgson, K. O., Borovik, A. S., Baker, M. L. & Solomon, E. I. "X-ray Spectroscopic Study of the Electronic Structure of a Trigonal High-Spin Fe(IV) horizontal lineO Complex Modeling Non-Heme Enzyme Intermediates and Their Reactivity" *J Am Chem Soc*, **145**, 18977-18991 (2023).
19. Roemelt, M., Beckwith, M. A., Duboc, C., Collomb, M. N., Neese, F. & DeBeer, S. "Manganese K-edge X-ray absorption spectroscopy as a probe of the metal-ligand interactions in coordination compounds" *Inorg Chem*, **51**, 680-687 (2012).